

Contact-based Bridge Inspection Multirotors: Design, Modelling and Control Considering the Ceiling Effect

A.E. Jimenez-Cano, P.J. Sanchez-Cuevas, P. Grau, A. Ollero and G. Heredia

Abstract— This paper presents the design, modelling and control of a multirotor for inspection of bridges with full contact. The paper analyzes the aerodynamic ceiling effect when the aerial robot approaches the bridge surface from below, including its aerodynamic characterization using Computational Fluid Dynamics (CFD). The proposed multirotor design takes the modelled aerodynamic effects into account, improving the performance of the aerial platform in terms of the stability and position accuracy during the inspection. Nonlinear attitude and position controllers to manage the aerodynamic effects are derived and tested. Last, outdoor experiments in a real bridge inspection task have been used to validate the system, as well as, the controller and the aerodynamic characterization. The experiments carried out also include a complete autonomous mission of the aerial platform during a structural assessment application.

Index Terms—Aerial Systems: Applications; Aerial Systems: Mechanics and Control

I. INTRODUCTION

IN the last decade, the interest in the applications of the UAVs is growing exponentially [1]. Traditionally, UAVs have been used with a perceptive role in most applications, such as exploration, mapping and localization. However, the recent appearance of aerial manipulators, in which the aerial robots are able to physically interact with the environment, significantly increases the variety of the tasks [2][3].

The operations of these autonomous aerial robots are ranging from the inspection and maintenance of industrial facilities [4][5] to the assessment of big structures in post-disaster situations [6], such as earthquakes or man-made extreme events. In [7] and [8] the authors evaluated the feasibility of carrying out bridge inspections using UAVs which establish a full contact condition with the bridge.

Although the use of aerial robots for bridge inspection is not widely extended, the interest in this technology is growing significantly in previous years [9]. For instance, in [10] UAVs have been used for carrying out visual inspection and in [8] the authors proposed the use of aerial vehicles, that are able to touch and even maintain the contact with the bridge, increasing the use of the aerial robots in different applications.

Manuscript received: February, 23, 2019; Accepted June, 27, 2019.

This paper was recommended for publication by Editor Jonathan Roberts upon evaluation of the Associate Editor and Reviewers' comments.

A.E. Jimenez-Cano (antenr@us.es), P.J. Sanchez-Cuevas (psanchez16@us.es), P. Grau (pegrau@us.es), A. Ollero (aollero@us.es) and G. Heredia (guiller@us.es) are with the Robotics, Vision and Control Group at the University of Seville, Spain.

Digital Object Identifier (DOI): see top of this page.

These tasks require physical interaction between the aerial robot and the environment and produce significant changes in the dynamic behavior of the aerial platform. For aerial manipulators, these changes are usually due to the movement of the manipulator which could produce variations in both the aerial vehicle mass center and the inertial characteristics [11][12]. But, in case of aerial robots that fly very close to structures and obstacles, the behavior of the aircraft changes as a consequence of aerodynamic disturbances [13]. Both problems have been preliminarily studied in the literature, for instance, [14] and [15] present a control scheme which takes into account the movement of the arm of aerial manipulators while [16] is focused on the controller of multirotors working close to ground surfaces. External wrench observers [17] have been used to estimate unknown forces and torques acting on the multirotor, and design controllers for the aerial robot [18]. These observers could be used to estimate these aerodynamic effects, although when the multirotor approaches the surfaces there are large gradients in the generated forces, and wrench observers are not well suited for estimating fast varying forces.

The problem of UAVs flying close to obstacles that act as a ceiling surface has not been studied in detail. The ceiling effect appears when the aerial platform is flying close enough to a horizontal surface from below. This situation, that happens during inspection of the beams of a bridge, produces changes in the flow field that significantly increase the thrust generated by the rotor. An important point is that while in the ground effect (the multirotor flying *over* a surface close to it) the increment in rotor thrust takes the UAV away from the surface, and thus it is “safe” [16], in the ceiling effect (the multirotor flying *below* a surface close to it) the increment in rotor thrust moves the UAV against the surface, and thus can be dangerous and cause a crash with the ceiling. For this reason, it is important to consider it in the design of the aerial robot and the control scheme.

Although previous studies about the ceiling effect have been presented in [7] and [19], these have been analyzed only from an experimental point of view. The first contribution of this paper consists of analyzing the ceiling effect using CFD simulations that can be easily extended to any type of multirotor configuration. These results have been used in the design of a multirotor which is able to exploit the ceiling effect to improve its performance during operation. The second contribution of this paper is the derivation of a multirotor controller that takes into account explicitly the ceiling effect and allows it to fly very close to the bridge beams in safe conditions. Moreover, the proposed solution

improves the performance of the aerial platform and has been tested during a series of outdoor experiments in a real bridge inspection (see Figure 9, [22] and Section V.E). This paper also presents a new design of a lightweight multirotor platform and the hardware/software architecture that is necessary to carry out the bridge inspection by contact.

The rest of the paper is organized as follows: Section II describes the aerodynamic analysis accomplished to model the ceiling effect. Section III presents the dynamic model of the multirotor considering the aerodynamic ceiling effect which has been previously characterized. Section IV explains the control system and the experimental results are presented in Section V where are also presented the final hardware/software architecture implemented. Finally, conclusions are included in Section VI.

II. AERODYNAMIC ANALYSIS FOR PLATFORM DESIGN

A. Problem Statement

Nowadays, the structural assessment of bridges involves the use of much equipment, including heavy machinery like lifters, scaffolders and cranes among others. Moreover, although one part of this assessment is a visual inspection to detect cracks, corrosion, leaching and other defects, other tasks require direct contact of a sensor with the structure of the bridge. The contact tasks are usually carried out by an operator that manually places sensors on the bridge to obtain different measurements, such as crack depth or beam deflection. For bridge beam deflection, the most used solution is to place a reflector prism in contact with the bridge and its position is measured with a laser total station on the ground. This task is not just hard and slow, due to the use of specified machinery when the bridge environment is very complex, but it is also dangerous for the operators.

This paper describes the system developed to accomplish the bridge inspection by contact in safety conditions using UAVs. Thanks to the design proposed, the aerodynamic effects, that arise flying close to the bridge, can be exploited to improve the main performances of the aircraft, such as, the power consumption and the accuracy during the inspection task.

The inspection system was preliminarily presented in [7] and consist of an aerial platform that acts as a flying sensor with the capability of touching and maintaining a contact with the bridge, a reflector prism on-board and a robotic total station to take the measurements during the inspection and, finally, a Ground Control System (GCS) to monitor the state of the aircraft and supervise the state of the inspection. This paper also the nonlinear control scheme in Sections III and IV that allows accomplishing the bridge inspection in an autonomous way, also makes use of the CFD analysis.

B. Aerodynamic Analysis of the Ceiling Effect

The aerodynamics of single rotors has been widely studied in the helicopter literature. A simple model of a rotor flying in ground effect has been proposed, which is based on potential flow modelling the rotor as a point source and using the method of images [20]. This model is not valid for multirotors since the geometry of the frame modifies significantly the airflow close to the ground. The authors have proposed a model for the ground effect based on potential flow and

adding an additional experimental factor that depends on the platform geometry [16].

Although a similar potential flow model can be formulated for the ceiling effect, it does not agree with experimental results even for a single rotor, suggesting that the physical mechanism is different in the ceiling effect. The authors have analyzed experimentally the aerodynamic ceiling effect for different multirotor configurations [7][8], showing that the application range of these works is limited to the specific design of the multirotor studied because the aerodynamic effect heavily depends on the aerial platform geometry. Therefore, this paper assesses and models the aerodynamic ceiling effect on the quadrotor using CFD to optimize the performance of the aircraft during the inspection. CFD simulations have been done with ANSYS and its own modules for meshing, solver (Fluent) and post-processing results.

1) CFD setup

a) Meshing

Figure 1 shows the complete geometry of the proposed aircraft and the simulated mesh. The two symmetry planes are defined in ANSYS Fluent as symmetry boundary conditions.

Therefore, the modeled domain is reduced to a portion of 1/4th, improving calculation times without any loss in accuracy.

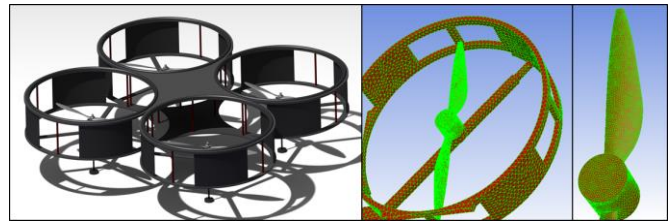


Figure 1 Geometry and mesh detail

Different meshes have been done at different distances between the propeller and the ceiling surface, ranging from 4cm (at this distance, the quadrotor frame touches the ceiling) to 50cm. The number of elements of these meshes is about 2e6. The mesh is composed of tetrahedral elements and is refined in the proximities of the propeller, where the solution is required to be accurate.

b) Solver Settings

First, the turbulence model used in this case was the “k-ε Realizable”. Second, the equations employed to solve the problem are the mass, momentum and energy conservation. Third, the fluid is modelled as an ideal gas. Last, boundary conditions are defined as follows: the propeller is a wall with no-slip condition which rotates around its axis. The frame and the top surface of the domain (ceiling) are considered as stationary walls with no-slip condition. The lateral and bottom limits of the area are both defined at constant pressure and temperature of 1atm and 300K to emulate far-away flow field conditions. Both symmetry planes are established as symmetry boundary condition.

A transient simulation is solved to take into account the movement of the propeller. The time step is chosen to be equivalent to a 1/10th of a propeller complete revolution, so it

varies between simulations where the angular speed of the propellers changes. For each time step, the software iterates until convergence is reached. This process continues for 10 propeller complete revolutions to ensure stable results.

2) Methodology

Previous results [7] have shown that the ceiling effect not only increases the thrust but also changes the velocity of the rotors (RPM). This is due to the suction that arises when the rotors work very close to the ceiling which decreases the air pressure around the propellers and the power consumed by the rotors. Most electronic speed controllers work sending PWM signals to the rotors and do not have closed-loop speed control, so they cannot compensate this effect. So, this problem is analyzed as follows to properly model the ceiling effect:

For a quadrotor in free flight conditions, the relations between thrust T , angular speed Ω , and power consumed P on each rotor have been assumed in the literature as:

$$T(\Omega) = C_T \Omega^2$$

$$P(T) = K_P T^{1.5}$$

In these expressions, C_T and K_P are constants whose value only depend on the geometry of the propeller (diameter, pitch, airfoil distribution) and the ambient conditions (air density, relative humidity). However, if the platform flies close to an obstacle, these expressions are no longer valid. In the case of use of this work, these variables also change with the distance to the ceiling when the aircraft flies close to the bridge.

To model this ceiling effect, two assumptions can be made:

Assumption 1: 1) C_T and K_T do not remain constant but are functions of the distance from the propeller to the ceiling z . 2) C_T and K_T remain independent of the angular speed Ω .

Assumption 2: The relations between T, P and Ω remain unchanged.

Both assumption 1 and assumption 2 will be validated using CFD in the next section. Then, the classical approach of T and P can be reformulated as follows:

$$T_{ICE}(z, \Omega) = C_{T_{ICE}}(z) \Omega^2$$

$$P_{ICE}(z, T) = K_{P_{ICE}}(z) T^{1.5}$$

Therefore, the ceiling effect is modelled through the functions $C_T(z_i)$ and $K_T(z_i)$ and then it is assumed that the thrust can be modeled as:

$$T_{ICE}(z, \Omega) = K_c(z) C_{T_{OCE}} \Omega^2$$

3) CFD Results

Several CFD simulations were performed to validate the assumptions of the previous sections. These simulations consisted of assessing the behavior of a quadrotor in terms of thrust, T , and power, P . More than 30 different simulations for different distances and RPM were performed. The qualitative behavior of the flow field can be explained with the two simulations presented in Figure 2

In Figure 2.a the quadrotor is touching the ceiling and in Figure 2.b it is placed at 10cm of the ceiling. Then, when rotating, the propellers (in black in Figure 2) take the upstream air and accelerates it downwards. In the presence of the ceiling, the air movement is restricted, and a low-pressure bubble also appears between the rotor and the ceiling. Thus,

the air particles close to the ceiling and in the proximities of the propeller are attracted to the rotor area and accelerated downwash. Far away from the propeller, the fluid remains unaltered (deep blue).

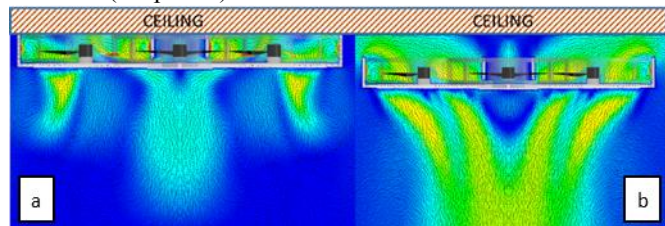


Figure 2 Velocity field when the multirotor is: a) in contact with the ceiling; b) flying 10 cm below the ceiling.

Assuming the distance to the ceiling as $z = z_j$ and the angular speeds as $\Omega = \Omega_k$. The equations of the assumptions 1 and 2 become linear when taking logarithms:

$$\log T_{jk} = \log C_{T_{ICE},jk} + 2 \log \Omega_k$$

$$\log P_{jk} = \log K_{T_{ICE},jk} + 1.5 \log T_{jk}$$

Thus, and due to the CFD simulations provide a complete solution of the flow field of the problem, it is possible to validate these expressions and for consequence the assumption 2. This has been done calculating the values of the exponents in the expressions of assumption 2 through the values of T, C_T, P and K_P provided by the CFD. The results are presented in the table below and validate the relations between T, P and Ω . Assumption 1 is validated through the results presented in Figure 3 and Figure 4 for different rotation velocities, where it can be clearly seen that the ceiling effect does not depend on the RPM.

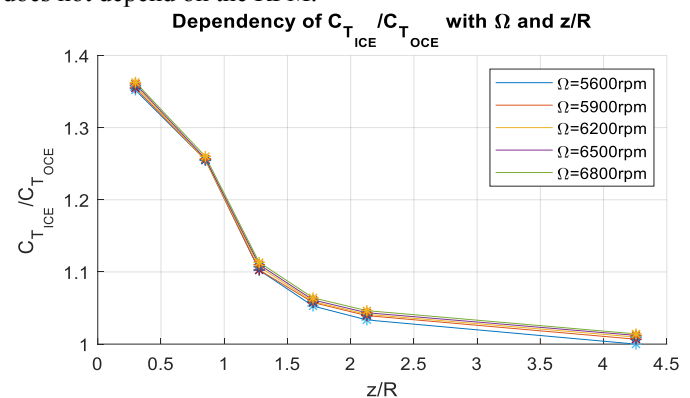


Figure 3 C_T vs z/R for different RPMs

Model	Exp. Mean value	Exp. Standard deviation
$T_{ICE}(z, \Omega) = C_{T_{ICE}}(z) \Omega^2$ -Exp 2	2.0487	0.0178
$P_{ICE}(z, T) = K_{P_{ICE}}(z) T^{1.5}$ -Exp 1.5	1.4796	0.0482

Last, Figure 5 shows the results of $K_c(z)$ that appear when the rotors approach the ceiling assuming that the power is constant. This model, that is represented by the yellow dashed line in Figure 5, has been compared with previous results with other platforms [7], showing that the designed platform exploits the ceiling effect in a more effective way than previous designs.

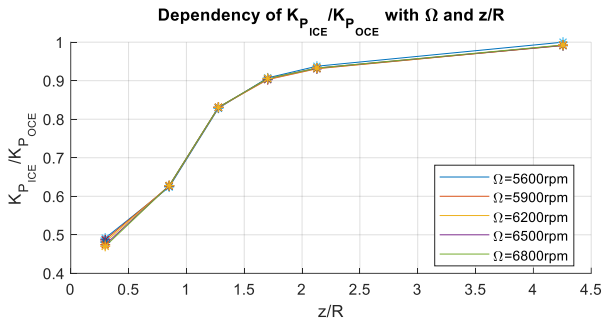
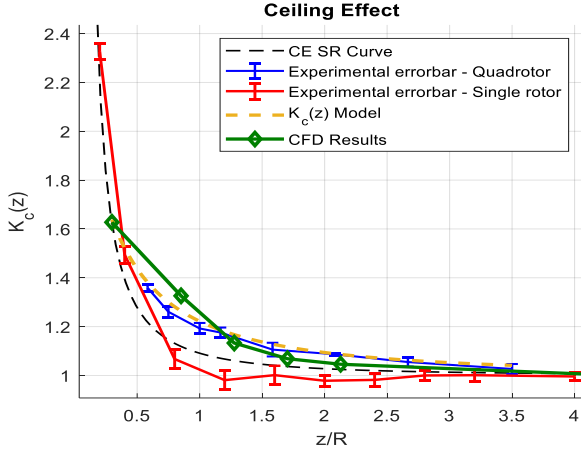

 Figure 4 K vs z/R for different RPMs


Figure 5 CFD – Experimental Results Comparison. Blue error bar and red errorbar are experimental results for quadrotor and multirotor respectively. Black braked line is the model proposed in [7] for the single rotor in ceiling effect. Yellow braked line is the model used in this work for the aerial platform designed (eq. 2).

For this platform, K_c is modeled as:

$$K_c(z) = \frac{1}{1 - \frac{1}{a_1} \left(\frac{R}{a_2 + z} \right)^2} \quad (1)$$

Both, $a_1 = 0.081$ and $a_2 = 1.026$ are values obtained through least squares minimizing the error with the CFD results.

III. DYNAMIC MODEL WITH AERODYNAMIC EFFECTS

The dynamic model of a quadrotor is widely known in bibliography [21]. Thus, defining a set of generalized coordinates as $\xi = [x \ y \ z \ \phi \ \theta \ \psi]^T$, and considering the ceiling effect, the dynamic model of a quadrotor is described by the following equations,

$$\ddot{\xi} = \begin{bmatrix} 0 \\ 0 \\ -g \\ \dot{\theta}\dot{\psi} \left(\frac{I_y - I_z}{I_x} \right) - \frac{J_r}{I_x} \dot{\theta}\dot{\Omega} \\ \dot{\phi}\dot{\psi} \left(\frac{I_z - I_x}{I_y} \right) + \frac{J_r}{I_y} \dot{\phi}\dot{\Omega} \\ \dot{\phi}\dot{\theta} \left(\frac{I_x - I_y}{I_z} \right) \end{bmatrix} + \begin{bmatrix} \frac{1}{m} I_3 & 0 \\ 0 & \alpha \mathbb{I}^{-1} \end{bmatrix} F(\xi) + F_e \quad (2)$$

with

$$\alpha = \begin{bmatrix} d & 0 & 0 \\ 0 & d & 0 \\ 0 & 0 & 1 \end{bmatrix}, \mathbb{I} = \begin{bmatrix} I_x & 0 & 0 \\ 0 & I_y & 0 \\ 0 & 0 & I_z \end{bmatrix}, I_3 = \begin{bmatrix} 1 & 0 & 0 \\ 0 & 1 & 0 \\ 0 & 0 & 1 \end{bmatrix} \quad (3)$$

$$\Omega = \Omega_1 - \Omega_2 + \Omega_3 - \Omega_4$$

Here, g is the gravity, d is the distance between the geometric center of the quadrotor and the center of a rotor, $I_i (i = x, y, z)$ are diagonal terms of the inertia matrix, m is the aerial vehicle total mass and J_r is the rotor moment of inertia. Vector $F(\xi)$ encompasses actuator forces and torques exerted by the rotors. These forces and torques depend on the state of the multirotor due to the aerodynamic effects. Last, F_{ext} includes external forces and torques which are not known or modelled, such as contact forces or wind disturbance. The mass matrix and the gravity vector are the same that have been widely presented for the literature, but in this case, and due to the flight conditions, the force vector acting on the vehicle is:

$$F(\xi) = \begin{bmatrix} (c_\phi s_\theta c_\psi + s_\phi s_\psi) T(\xi) \\ (c_\phi s_\theta s_\psi - s_\phi c_\psi) T(\xi) \\ c_\phi c_\theta T(\xi) \\ \tau_\phi(\xi) \\ \tau_\theta(\xi) \\ \tau_\psi(\xi) \end{bmatrix} \quad (4)$$

where $c_\alpha = \cos(\alpha)$, $s_\alpha = \sin(\alpha)$ and (ϕ, θ, ψ) are the Euler angles. Defining the total thrust $T(\xi)$, as $T(\xi) = \sum_{i=1}^4 T_i(\xi)$, and taking into account that the platform is a quadrotor in cross configuration, there is a direct correspondence between the four generalized moments and the angular velocities of the rotors in which the vector $F(\xi)$ follows (4) where the aerodynamic ceiling effect has been included.

$$\begin{bmatrix} T \\ \tau_\phi \\ \tau_\theta \\ \tau_\psi \end{bmatrix} = \begin{bmatrix} K_c(z_{c_1})c_T & K_c(z_{c_2})c_T & K_c(z_{c_3})c_T & K_c(z_{c_4})c_T \\ -K_c(z_{c_1})dc_T & K_c(z_{c_2})dc_T & K_c(z_{c_3})dc_T & -K_c(z_{c_4})dc_T \\ K_c(z_{c_1})dc_T & -K_c(z_{c_2})dc_T & K_c(z_{c_3})dc_T & -K_c(z_{c_4})dc_T \\ c_D & c_D & -c_D & -c_D \end{bmatrix} \begin{bmatrix} \Omega_1^2 \\ \Omega_2^2 \\ \Omega_3^2 \\ \Omega_4^2 \end{bmatrix} \quad (5)$$

where z_{c_i} is the distance from the i -rotor to the ceiling defined as follows:

$$\begin{aligned} z_{c_1} &= z_c - \frac{\sqrt{2}}{2} d (\sin(\theta) - \cos(\theta) \sin(\phi)) \\ z_{c_2} &= z_c - \frac{\sqrt{2}}{2} d (-\sin(\theta) + \cos(\theta) \sin(\phi)) \\ z_{c_3} &= z_c - \frac{\sqrt{2}}{2} d (\sin(\theta) + \cos(\theta) \sin(\phi)) \\ z_{c_4} &= z_c - \frac{\sqrt{2}}{2} d (-\sin(\theta) - \cos(\theta) \sin(\phi)) \end{aligned} \quad (6)$$

where z_c is the distance from the center of gravity of the multirotor to the ceiling.

IV. CONTROL

In this section, we present a nonlinear Lyapunov-based attitude, altitude and position controllers for bridge inspection flights. The main goal of the designed controller is that the quadrotor can fly very close to the beams and carry out contact tasks with safety and accuracy. The ceiling effect is the most critical aerodynamic effect occurring during these inspection tasks. In the previous section, the ceiling effect has been modelled and introduced in the system's equations of motion. The relationship between the control inputs and the angular velocities of the rotors have been shown in equation (5). In this expression, the z_{c_i} of each rotor has been calculated to obtain the ceiling effect for each one. Depending of the multirotor attitude, the ceiling effect is different in each rotor. As Figure 6 shows, if the aircraft has a pitch angle about ± 10 degrees (flight forward), the aerodynamic ceiling effect is

approximately a 22% higher in one rotor than in the other when $z_c = 0.1$ m. However, it decreases to 5% when the attitude angles are about ± 3 degrees. Furthermore, it decreases to 2% when $z_c = 0.25$ m. This result implies that it is possible to make the following assumptions to increase the safety during the operation:

Assumption 3: 1) A forward flight will be done to a minimum distance of 0.25 m. to the ceiling surface. 2) The only operation allowed for distances less than 0.25 m will be the hover until reaching the contact with the surface.

Taking into account the assumption 3, equation (1) is linearized in intervals in which the difference between the aerodynamic effects is less than 5% and therefore $z_c \sim z_{c1} \sim z_{c2} \sim z_{c3} \sim z_{c4}$.

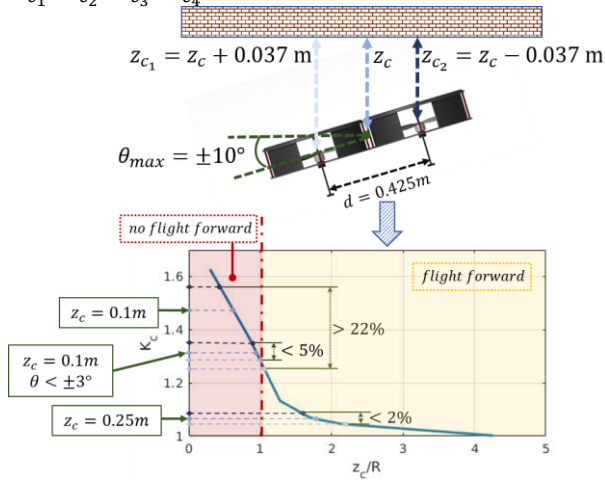


Figure 6 Response of a multirotor in ceiling effect and safety flight envelope.

Thus, the expression for the control inputs (5) can be simplified as follows:

$$U = \begin{bmatrix} K_C(z_c) & 0 & 0 & 0 \\ 0 & K_C(z_c) & 0 & 0 \\ 0 & 0 & K_C(z_c) & 0 \\ 0 & 0 & 0 & 1 \end{bmatrix} \begin{bmatrix} c_T & c_T & c_T & c_T \\ -dc_T & dc_T & dc_T & -dc_T \\ dc_T & -dc_T & dc_T & -dc_T \\ c_D & c_D & -c_D & -c_D \end{bmatrix} \begin{bmatrix} \Omega_1^2 \\ \Omega_2^2 \\ \Omega_3^2 \\ \Omega_4^2 \end{bmatrix} \quad (7)$$

Then,

$$\begin{bmatrix} T \\ \tau_\phi \\ \tau_\theta \\ \tau_\psi \end{bmatrix} = \begin{bmatrix} K_C(z_c) & 0 & 0 & 0 \\ 0 & K_C(z_c) & 0 & 0 \\ 0 & 0 & K_C(z_c) & 0 \\ 0 & 0 & 0 & 1 \end{bmatrix} \begin{bmatrix} U_z \\ U_\phi \\ U_\theta \\ U_\psi \end{bmatrix} \quad (8)$$

A. Nonlinear Attitude Controller

Attitude control keeps the stabilization of the aerial platform and the desired 3D orientation needed to track a desired path. As the derivation is similar for roll, pitch and yaw angles controller, only roll controller formulation will be presented. First, let us define the tracking error and speed tracking error as,

$$e_\phi = \phi - \phi_d \quad (9)$$

$$e_{\dot{\phi}} = \dot{\phi} - \dot{\phi}_d + k_\phi e_\phi \quad (10)$$

The stability of the roll controller is checked defining a Lyapunov function. Then we propose the candidate Lyapunov function, V_ϕ , defined as,

$$V_\phi = \frac{1}{2}(e_{\dot{\phi}}^2 + e_\phi^2) \quad (11)$$

Both angular tracking and speed tracking errors have been included in the candidate Lyapunov function. Thus, deriving (11) and using (2) gives,

$$\begin{aligned} \dot{V}_\phi &= e_\phi \dot{e}_\phi + e_{\dot{\phi}} \dot{e}_{\dot{\phi}} \\ &= e_\phi (e_{\dot{\phi}} - k_\phi e_\phi) + e_{\dot{\phi}} (\dot{\phi} - \ddot{\phi}_d + k_\phi (e_{\dot{\phi}} - k_\phi e_\phi)) \\ &= e_\phi (e_{\dot{\phi}} - k_\phi e_\phi) + e_{\dot{\phi}} \left(\dot{\theta} \psi \left(\frac{I_y - I_x}{I_x} \right) - \frac{J_r}{I_x} \dot{\theta} \Omega \right. \\ &\quad \left. + \frac{dK_C(z_c)}{I_x} U_\phi - \ddot{\phi}_d + k_\phi (e_{\dot{\phi}} - k_\phi e_\phi) \right) \end{aligned} \quad (12)$$

Now, in order to guarantee the stability of \dot{V}_ϕ , it should be seminegative definite, thus the control input for roll attitude is given by,

$$U_\phi = \frac{I_x}{dK_C(z_c)} \left(\dot{\theta} \psi \left(\frac{I_y - I_x}{I_x} \right) - \frac{J_r}{I_x} \dot{\theta} \Omega + (k_\phi^2 - 1) e_{\dot{\phi}} - (k_\phi + k_\phi) e_\phi \right) \quad (13)$$

where k_ϕ and $k_{\dot{\phi}}$ are positive constants. Therefore, using (13) in (12) results

$$\dot{V}_\phi = -k_\phi e_{\dot{\phi}}^2 - k_{\dot{\phi}} e_\phi^2 \leq 0 \quad (14)$$

As a result, global asymptotic stability is guaranteed due to the positive definition of V_ϕ , the fact that $\dot{V}_\phi < 0$, $\forall (e_\phi, e_{\dot{\phi}}) \neq 0$ and $\dot{V}_\phi(0) = 0$ and by applying LaSalle theorem. Following the same steps, the control inputs for pitch and yaw are given by,

$$U_\theta = \frac{I_y}{dK_C(z_c)} \left(\dot{\phi} \psi \left(\frac{I_x - I_z}{I_y} \right) + \frac{J_r}{I_y} \dot{\phi} \Omega + (k_\theta^2 - 1) e_{\dot{\theta}} - (k_\theta + k_\theta) e_\theta \right) \quad (15)$$

$$U_\psi = I_z \left(\dot{\phi} \dot{\theta} \left(\frac{I_x - I_y}{I_z} \right) + (k_\psi^2 - 1) e_{\dot{\psi}} - (k_\psi + k_\psi) e_\psi \right) \quad (16)$$

B. Nonlinear Altitude Controller

In the first step to design the proposed altitude controller, the tracking error and the speeds tracking error are defined as follows:

$$e_z = z - z_d \quad (17)$$

$$e_{\dot{z}} = \dot{z} - \dot{z}_d + k_z e_z \quad (18)$$

Where k_z is a positive constant. Thanks to the error definitions (17) and (18), it is possible to define a candidate Lyapunov function V_z to stabilize the altitude control system as follows:

$$V_z = \frac{1}{2}(e_{\dot{z}}^2 + e_z^2) \quad (19)$$

Then, deriving the equation (19), and using the equation (2) gives:

$$\begin{aligned} \dot{V}_z &= e_z \dot{e}_z + e_{\dot{z}} \dot{e}_{\dot{z}} \\ &= e_z (e_{\dot{z}} - k_z e_z) + e_{\dot{z}} \left(\frac{c\theta c\phi K_C(z_c)}{m} U_z - g - \ddot{z}_d \right. \\ &\quad \left. + k_z (e_{\dot{z}} - k_z e_z) \right) \end{aligned} \quad (20)$$

Assuming that the ceiling effect function is positive (see Figure 5, $K_C(z_c) \geq 1, \forall z_c \in \mathbb{R}$, and $\ddot{z}_d = 0$, then, due to the error definitions and according to the Lyapunov stability theorem, the control input, U_z , is defined as follows:

$$U_z = \frac{m}{c\theta c\phi K_C(z_c)} (g + (k_z^2 - 1) e_z - (k_z + k_z) e_{\dot{z}}) \quad (21)$$

Where k_z is a positive constant. Using the equation (21) in (20), the time derivative of the candidate Lyapunov function is rewritten as:

$$\dot{V}_z = -k_z e_{\dot{z}}^2 - k_z e_z^2 \leq 0 \quad (22)$$

equation (22) holds if and only if (21) exists. Then, both attitude angles, roll and pitch, should be bounded between $-\frac{\pi}{2}$ and $\frac{\pi}{2}$. Keeping this condition, \dot{V}_z is seminegative definite and the altitude control is asymptotically stable. The proposed altitude control presents two advantages. The first one is to keep the altitude during a flight forward when $R/z_c > 1$ and therefore $K_c(z_c) \approx 1$. The second one is during a contact mission. In this case, the attitude angles, roll and pitch, should be small and when the multirotor is flying close to the ceiling, the function $K_c(z_c)$ should increase and the multirotor should be able to keep the altitude as well as reducing the thrust input and therefore, minimizing the energy consumption.

C. Nonlinear Position Controller

In underactuated systems like the quadrotors, the horizontal motion is achieved by rotating the quadrotor towards the desired direction. Thus, the position control is responsible for commanding the desired roll and pitch angles to attitude controller. Following the steps of previous subsections, let define the position tracking and speed tracking errors as:

$$e_x = x - x_d \quad (23)$$

$$\dot{e}_x = \dot{x} - \dot{x}_d + k_x e_x \quad (24)$$

$$e_y = y - y_d \quad (25)$$

$$\dot{e}_y = \dot{y} - \dot{y}_d + k_y e_y \quad (26)$$

Then, the control laws are given by,

$$U_x = \frac{m}{U_z} ((k_x^2 - 1)e_x - (k_x + k_{\dot{x}})\dot{e}_x) \quad (27)$$

$$U_y = -\frac{m}{U_z} ((k_y^2 - 1)e_y - (k_y + k_{\dot{y}})\dot{e}_y) \quad (28)$$

The generated position control signals are used to obtain the desired roll, ϕ_d , and pitch angles, θ_d .

V. EXPERIMENTAL RESULTS

A. Hardware/Software Description

This section describes the system used in the experiments outdoors, which is shown in Figure 7.



Figure 7 System overview. a) Aerial Platform. b) Reflector Prism. c) GCS. d) Robotic total station

Figure 7.a shows the platform used during the experiments, which is a cross layout quadrotor with the propulsive system and the avionics onboard covered in a full carbon fiber frame. Furthermore, this aerial platform is designed to exploit the benefits of the ceiling effect as was explained in Section II. The propulsive system consists of DJI 2312E rotors with 9" propellers DJI and 420Lite ESC and the onboard avionics consist of a custom autopilot code running in a Raspberry Pi 3 Model B connected to the Emlid's sensors shield Navio2. This hardware supports Wi-Fi technology that has been used to link the ground control station (Figure 7.c) with the aerial platform. In addition, the platform also mounts a range sensor SF11/C LIDAR connected through the I2C bus.

Figure 7.d and Figure 7.b show the robotic total station (Leica Geosystem MS50) and the reflector prism (GRZ 360°

mini-prism) used to accomplish the measurements during the inspection and to estimate the position of the aircraft during the flight in the position control loop. The accuracy of these measurements is about 1 cm in flight and increase during the contact inspection to 0.1mm. The maximum frequency of the measures is 20 Hz.

The hardware/software architecture is presented in Figure 8. This scheme shows that the autopilot is connected to the GCS through Wi-Fi link. The robotic total station is also connected to the GCS through a serial port. The GCS receives the prism position and sends it to the aerial platform, acting as a bridge between the robotic total station and the aerial platform. However, the measurements of the total station are treated and filtered onboard for safety conditions.

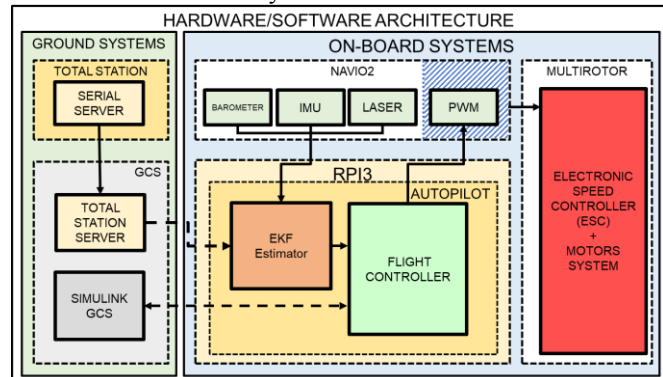


Figure 8 Hardware/software architecture. WiFi communication is represented by dashed arrows and wired communication by the bold arrows.

B. Experiments overview



Figure 9 Navas bridge and experiment overview

The system has been tested in different experiments in the "Navas bridge" at Algodonales, Cadiz, Spain (Figure 9). The experiments started with piloted test in which the human pilot approaches the multirotor to bridge surface in order to obtain a first result of the aircraft behavior on the proximity of the bridge. Next, the nonlinear controller was tested followed by a full autonomous mission which emulates the inspection procedure during a structural assessment task. Figure 9 also shows the aerial platform during a contact inspection. A video of the autonomous experiments can be found on [22].

C. Manual Flight Results

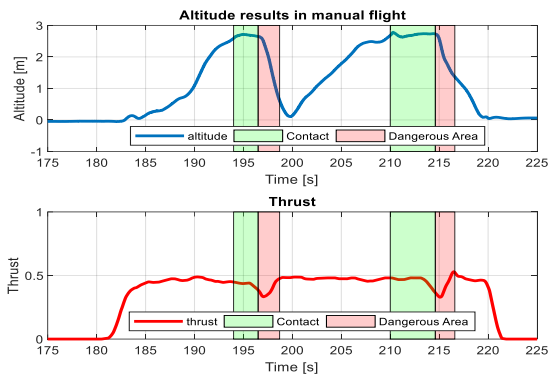


Figure 10 Altitude telemetry results during in manual flight. Red zone represents the dangerous area in which the aircraft critically loses its altitude and it could generate a dangerous flight condition

First experiments, which were carried out piloted by a human, show that the aircraft is very unstable at the end of the contact phase. The results in Figure 10 show that the pilot must significantly decrease the thrust signal at least until 40% less than the thrust hover to finish the contact task. This situation leads to conditions in which the aircraft critically loses its altitude and it could generate a dangerous flight condition. Then, it becomes clear the need of implementing an automatic control strategy to fix this behavior. This is one of the main conclusions of this work.

D. Nonlinear Controller Results

The next experiment was accomplished with the automatic control strategy proposed in Section IV. In this case, the results of Figure 11 and Figure 12 show the altitude controller result, as well as, the values of the thrust, the aerodynamic ceiling effect estimation and the vertical velocity. These results reveal that the controller implemented allows the platform to fly in safe conditions when it approaches and moves away from the bridge surface. Moreover, Figure 11 also shows how the controller acts during the contact and in the second result, which is about the thrust commanded, it can be seen that, despite of the oscillations due to the error in the state estimation, the mean value of thrust (represented with the red dashed line) decreases as a consequence of taking into account the ceiling effect in the nonlinear controller.

It is important to remark that the most important benefits of this nonlinear control appears in the z -position and z -velocity controller. The result of Figure 12 shows the z -velocity controller results in which it can be observed that the nonlinear controller is faster and the un-stick command is followed in a more efficient way. For instance, this result clearly shows that the nonlinear controller easily follows the reference with a small delay (0.25 s) while a standard PID controller needs to integrate and accumulate too much error for following the reference (4 s) because this one does not take into account the aerodynamic ceiling effect. On the other hand, Figure 12 also presents the performance of the z -position controller. These results show that the linear controller is not only slower, but also is less safe due to the overshooting presented in the dangerous zone (red background) which does not appear with the proposed

nonlinear controller. Moreover, the reason why both controllers shows a small delay is due to the limits of the sensors used to estimate the position of the vehicle. The robotic total station provides very high positioning accuracy (~ 1 cm), but it has a delay and its update rate is time-varying and relatively low, limiting the performance of the nonlinear controller and causing a small delay in the response of the multirotor.

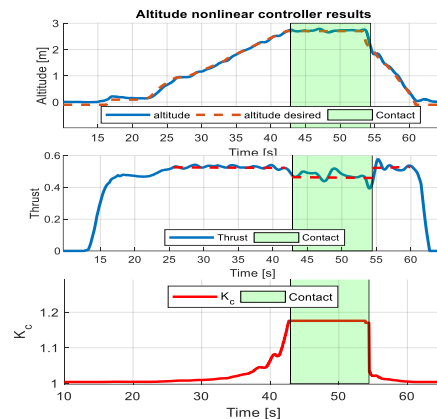


Figure 11 Altitude nonlinear controller results. Altitude vs altitude reference control, thrust and mean value during the flight and contact (red dashed), and estimation of the ceiling effect factor (K_c) during the flight.

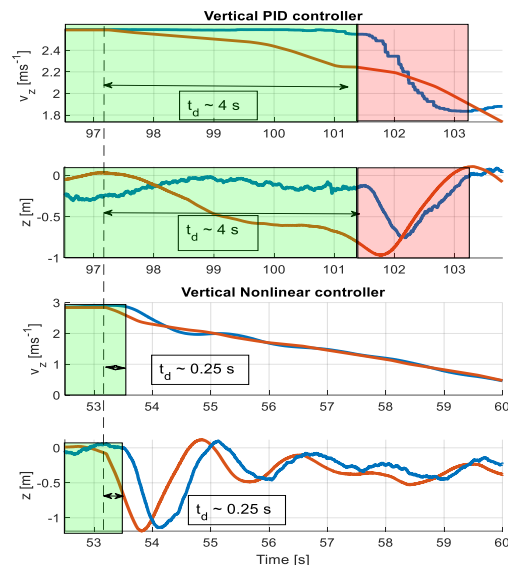


Figure 12 PID vs Nonlinear z -velocity and z -position controller comparison. Green backgrounds represent the contact condition; red background is the dangerous zone where it can be observed an overshooting. It is shown that the non-linear controller is more than 4 times faster moving away from the ceiling.

Next section shows a complete telemetry set of the multirotor flying in a bridge inspection where it is possible to assess the result of the controller along the flight.

E. Autonomous Inspection

Last experiments consisted of accomplishing a full inspection by contact in autonomous mode (see video in [22]). These results, which are presented in Figure 13 and Figure 14, show that the system is able to navigate between different contact points in safety conditions. In Figure 13, it can be seen

that the proposed z-position controller allows the aircraft to move away from the ceiling without entering dangerous flight conditions or losing critically their altitude, as it happens in Figure 10 (see red area in Figures 11, 13 and 14).

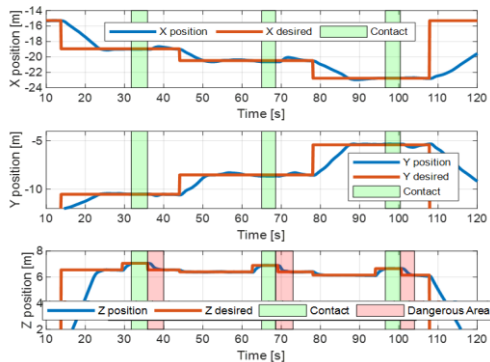


Figure 13 Position controller results during an autonomous mission.

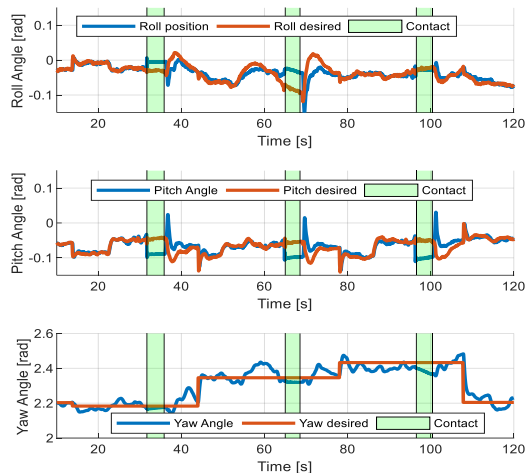


Figure 14 Attitude controller results during an autonomous mission

VI. CONCLUSION

This paper has presented the design, modeling and control of a multirotor which is able to fly very close to the ceiling surface and even establish a full contact with it for carrying out a bridge inspection by contact.

The design of the aerial platform was based on a detailed aerodynamic study of the ceiling effect performed with CFD. Thus, the aircraft can exploit the ceiling effect in its favor and do the inspection operation in a more effective way. This ceiling effect was also modeled through results of the CFD and it was included in the dynamic model of the quadrotor reformulating the classical approach of these equations. Moreover, the controller scheme used to accomplish the contact and fly close to the bridge surface have been described and implemented in a real platform.

Last, outdoor experiments in a real bridge have validated the proposed design, as well as the controller and the aerodynamic characterization even during a full autonomous mission. Future work related with this research will be focused on the end-user of this technology and the inspection application.

The aim of these works will be: increase the applicability of

this technology, increase its the technology readiness level (TRL), and, turn it in a competitive option in commercial exploitation

ACKNOWLEDGMENT

This work has been supported by the ARTIC Project, funded by the Spanish Ministerio de Economía, Industria, y Competitividad (RTI2018-102224-B-I00), the H2020 RESIST Project, funded by the European Commission (H2020-MG-2017-769066), the H2020 AEROBI Project, funded by the European Commission (H2020-ICT-2015-687384) and by the Spanish Ministerio de Educación, Cultura, y Deporte, FPU Program.

REFERENCES

- [1] Valavanis, K., and G. Vachtsevanos. "Handbook of Unmanned Aerial Vehicles", 2015.
- [2] Ruggiero, F., V. Lippiello, and A. Ollero. "Aerial manipulation: A literature review." IEEE RA-L 3.3 (2018): 1957-1964.
- [3] Fumagalli, M., et al. "Physical Interaction with the Environment." IEEE robotics & automation magazine 1070.9932/14 (2014).
- [4] Suarez, A., G. Heredia, and A. Ollero. "Lightweight compliant arm with compliant finger for aerial manipulation and inspection." IROS, 2016.
- [5] Kondak, K., et al. "Unmanned aerial systems physically interacting with the environment: Load transportation, deployment, and aerial manipulation." Handbook of Unmanned Aerial Vehicles. Springer, Dordrecht, 2015. 2755-2785.
- [6] Recchiuto, C.T., and A. Sgorbissa. "Post-disaster assessment with unmanned aerial vehicles: A survey on practical implementations and research approaches." Journal of Field Robotics 35.4 (2018): 459-490.
- [7] Sanchez-Cuevas, P. J., G. Heredia, and A. Ollero. "Multirotor UAS for bridge inspection by contact using the ceiling effect." ICUAS, 2017.
- [8] Sanchez-Cuevas, Pedro J., et al. "Robotic System for Inspection by Contact of Bridge Beams Using UAVs." Sensors 19.2 (2019): 305.
- [9] Chan, B., et al. "Towards UAV-based bridge inspection systems: A review and an application perspective." Structural Monitoring and Maintenance 2.3 (2015): 283-300.
- [10] Seo, J., L. Duque, and J. Wacker. "Drone-enabled bridge inspection methodology and application." Aut. in Const. 94 (2018): 112-126.
- [11] Pounds, P., D. Bersak, and A. Dollar. "Stability of small-scale UAV helicopters and quadrotors with added payload mass under PID control." Autonomous Robots 33.1-2 (2012): 129-142.
- [12] Mellinger, D., et al. "Design, modeling, estimation and control for aerial grasping and manipulation." IEEE/RSJ IROS 2011.
- [13] Powers, C., et al. "Influence of aerodynamics and proximity effects in quadrotor flight." Experimental robotics. Springer, Heidelberg, 2013.
- [14] Orsag, M., Christopher Korpela, and Paul Oh. "Modeling and control of MM-UAV: Mobile manipulating unmanned aerial vehicle." Journal of Intelligent & Robotic Systems 69.1-4 (2013): 227-240.
- [15] Jimenez-Cano, A. E., et al. "Control of an aerial robot with multi-link arm for assembly tasks." 2013 IEEE ICRA, 2013.
- [16] Sanchez-Cuevas, P., G. Heredia, and A. Ollero. "Characterization of the aerodynamic ground effect and its influence in multirotor control." International Journal of Aerospace Engineering 2017 (2017).
- [17] Tomic, T., C. Ott, S. Haddadin, "External wrench estimation, collision detection, and reflex reaction for flying robots," IEEE TRO, 33(6), pp. 1467 - 1482, 2017.
- [18] Ruggiero, F., J. Cacace, H. Sadeghian, V. Lippiello, "Passivity-based control of VTOL UAVs with a momentum-based estimator of external wrench and unmodeled dynamics," Robotics and Autonomous Systems, 72, pp. 139-151, 2015.
- [19] Conyers, S., M. Rutherford, and K. Valavanis. "An empirical evaluation of ceiling effect for small-scale rotorcraft." 2018 ICUAS, 2018.
- [20] I. Cheeseman and W. Bennett, "The effect of the ground on a helicopter rotor in forward flight," ARC R&M 3021, 1955.
- [21] Bouabdallah S. and R. Siegwart, "Full control of a quadrotor." IEEE/RSJ IROS, 2007, 153-158.
- [22] Video of the experiments: <https://hdvirtual.us.es/discovirt/index.php/s/qZzDXGf54pAmbRA>